# 3D Reconstruction of Emission and Absorption in Planetary Nebulae

Andrei Linţu[†1]     Hendrik P. A. Lensch[1]     Marcus Magnor[2]     Sascha El-Abed[1]     Hans-Peter Seidel[1]

[1]MPI Informatik, Germany     [2]TU Braunschweig, Germany

**Abstract**

*This paper addresses the problem of reconstructing the 3D structure of planetary nebulae from 2D observations. Assuming axial symmetry, our method jointly reconstructs the distribution of dust and ionized gas in the nebulae from observations at two different wavelengths. In an inverse rendering framework we optimize for the emission and absorption densities which are correlated to the gas and dust distribution present in the nebulae. First, the density distribution of the dust component is estimated based on an infrared image, which traces only the dust distribution due to its intrinsic temperature. In a second step, we optimize for the gas distribution by comparing the rendering of the nebula to the visible wavelength image. During this step, besides the emission of the ionized gas, we further include the effect of absorption and scattering due to the already estimated dust distribution. Using the same approach, we can as well start with a radio image from which the gas distribution is derived without absorption, then deriving the dust distribution from the visible wavelength image considering absorption and scattering. The intermediate steps and the final reconstruction results are visualized at real-time frame rates using a volume renderer. Using our method we recover both gas and dust density distributions present in the nebula by exploiting the distinct absorption or emission parameters at different wavelengths.*

Categories and Subject Descriptors (according to ACM CCS): I.4.10 [Image Processing and Computer Vision]: Image Representation - Volumetric I.3.8 [Computer Graphics]: Applications J.2 [Computer Applications]: Physical Sciences and Engineering - Astronomy

## 1. Introduction

All astronomical nebulae are seen by an observer on Earth from a single perspective. Physics can help us infer the spatial distribution of some of these objects, but a quantitative understanding of their shape can only be gained by reconstructing their 3D structure and visualizing the derived models. Recently, there is an increased interest in the graphics community in the field of astronomical simulations and visualizations. Recent works range from physically correct animations of nebulae for planetarium shows [NGN*01], to a specifically designed raycasting application for visualizing large scale datasets such as galaxy or star formation [KWAH06].

In this paper, we present an approach to reconstruct and visualize 3D volumes of planetary nebulae. In tomography, reconstruction is typically based on several 2D projections of the object to be reconstructed, observed from different directions. Provided there are enough 2D projections of the object of interest, the volume can be reconstructed using filtered back-projection, algebraic reconstruction [GBH70] or other available techniques [SAP*02, TBH06].There are, however, some cases where there is only one available 2D projection of the volume, e.g., when the observed phenomenon occurs only once. In our case, the nebulae are so distant from the observer that only one projection is available. In order to obtain a plausible reconstruction of the object's real 3D distribution, additional constraints are necessary. In this paper we constrain the solution in two ways: axis-symmetry and optical consistency at different wavelengths. This axis-symmetry is found naturally in many planetary nebulae (See Figure 2 for example) [MKHD04].

---

† lintu@mpii.de
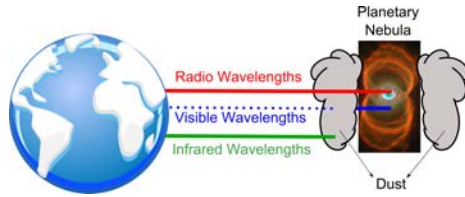
**Figure 1:** *Light in the* visible *wavelengths is partially absorped and scattered by dust present in the nebula.* Radio *wavelengths are not affected by any dust between the object and an observer on Earth. At certain* infrared *wavelengths, we can observe only the dust distribution in the nebula due to its blackbody radiation.*

Based on the symmetry constraint we present a method for reconstructing the 3D axis-symmetric distribution of an emissive volume containing participating media, and apply our technique to recover the structure of *planetary nebulae*. Our approach is based on the algorithm presented previously by Magnor et al. [MKHD04], who reconstructed only 3D emissive volumes for planetary nebulae. The authors assume that absorption and scattering is negligible. As pointed out in [Kwo00, LK05] there are, however, quite significant quantities of dust present in planetary nebulae and their effect needs to be considered. Therefore, we recover the 3D distribution of ionized gas *and* dust by extending the reconstruction algorithm in such a way that it also correctly accounts for absorption and scattering due to dust.

Since we need to optimize for two different distributions at the same time, a single input image is not sufficient. Our key contribution is to make use of the fact that the extinction coefficient of the dust particles is wavelength dependent. As input data we use two images recorded at different wavelengths, one radio image and one image in the visible spectrum, or similarly by using an infrared and a visible wavelength pair of images (See Figure 1). From physics follows that the radio image is almost unaffected by the dust present in the nebula. It can thus be used to estimate the emissive volume, i.e., the concentration of the ionized gas. From the recovered distribution one can then compute analytically how much light the nebulae would emit at visible wavelengths if no dust were present. Lee et al. [LK05] describe a simple way to compute the expected $H\alpha$ (emission line of ionized hydrogen) flux. By comparing this undisturbed estimate with the second recorded image at visible wavelengths, the dust distribution is derived. In a similar way, a pair of infrared and visible spectrum images can be used as input for our reconstruction algorithm, because infrared images trace mostly the dust distribution through its intrinsic temperature.

To visualize the reconstructed 3D volumes and the combined effect of ionized gas and dust we extend the real-time volume rendering approach for reflection nebulae described in [MHLH05]. Our visualization algorithm now considers *emission*, *scattering* and *absorption*, all at the same time.

The reconstructed volumes can be used by astronomers for visualizing and analyzing the 3D distribution of gas and dust in axis-symmetric nebulae, or for educational purposes in planetarium shows intended for the general public.

## 2. Planetary Nebulae

In this section we will briefly describe the physics behind planetary nebulae and discuss the effects of dust present in these astronomical objects. These nebulae form when a star of up to 5 times the mass of our Sun reaches the end of its life span. When the star runs out of hydrogen fuel for the nuclear reactions, its inner pressure decreases, causing it to collapse under its own gravity and to start heating up.

As the temperature around the central star is rising, ultraviolet photons are emitted which ionize the previously ejected gas surrounding the stellar core. Depending on the chemical elements present in the nebula, the emitted photons by the ionized gas have different energy levels, and thus generate light of different characteristic wavelengths. The emission in every such narrow band traces back the distribution of the corresponding chemical elements in the nebula. More in-depth information about the astrophysics of planetary nebulae can be found in [Kwo00, Ost74]. For a review on planetary nebula formation refer to [BF02].

A large number of these objects also show a distinct axial-symmetrical structure, Figure 2. This can be explained by the way some of these objects are created, which is mainly a strong jet of outflow of gas and dust in two opposite directions from the central star.

The electromagnetic radiation emitted by planetary nebulae, as presented in Figure 1, is affected differently depending on the wavelength the observations are conducted. At *visible* wavelengths, the dust present in the nebula absorbs and scatters the light reaching an observer on Earth. Whereas based on observations at *radio* wavelengths, the distribution of the ionized gas without the effects of scattering or absorption can be directly determined; we use this property in our reconstruction process, which is described in detail in Section 3.2.1. At *infrared* wavelengths (based on the laws of blackbody radiation), predominantly the dust particles present in the nebula emit electro-magnetic radiation caused by their intrinsic temperature. We use this property in our reconstruction process, which is described in detail in Section 3.2.2.

### 2.1. Absorption and Scattering

At visible wavelengths the dust particles in planetary nebulae affect the light reaching an observer on Earth by absorption and scattering. Even though the ionized gas in planetary nebulae emits light itself, the central star's emission is much brighter. Therefore, we consider the central star as being the only light source for the purpose of computing the amount
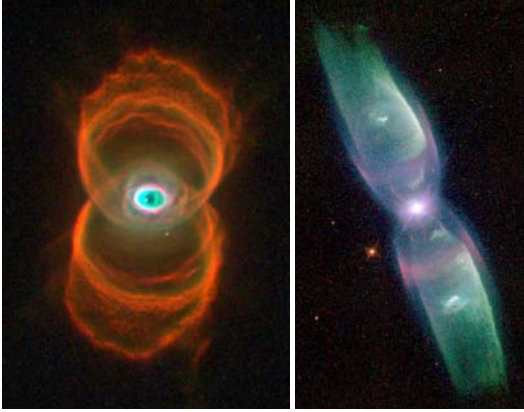
**Figure 2:** *Hubble Space Telescope Images of the Hourglass Nebula (left, courtesy of Sahai and Trauger (JPL), NASA) and the Butterfly Nebula (right, courtesy of Balick (University of Washington) et al., NASA). Both nebulae highlight significant axial symmetry. The Hourglass Nebula has a smaller inclination angle. Its symmetry axis is titled towards the viewer while for the Butterfly Nebular the axis is almost parallel to the image plane.*

of light scattered in the direction of the observer. The effect of absorption is given by the high amount of dust situated generally in the equatorial region of these objects, surrounding the central star, as well as the dust which is mixed with the ionized gas.

We create a physically-based model of light scattering in interstellar dust using two scalar parameters. First, there is *albedo*, which indicates how much light the particles reflect: 0 for total absorption, i.e., black dust, and 1 for the case when all incident light is scattered. The second parameter is the *single particle scattering probability* modeled using the Henyey-Greenstein phase function [HG41]. In addition, the presence of dust also attenuates any light shining through the dust region, which is described by the *extinction* parameter. Absorption is taken into account for light emitted by the ionized gas as well as the scattered light of the central star.

### 3. 3D Reconstruction

Our optimization is based on the following rendering model. The observed radiance $L(x,y)$ at a camera at position $c$ is a function of the gas emission $L_e(v)$, extinction $\tau(v)$, and the albedo $\sigma(v)$ of every voxel $v$ along the ray through the camera pixel:

$$L(x,y) = \int_c^\infty e^{-\int_c^v \tau(w)dw} \cdot (L_e(v) + \sigma(v) \cdot S(v)) \, dv, \quad (1)$$

where $S(v)$ is the total inscattering to the voxel $v$ towards the camera due to the emission $L_e^{star}$ of the nebula's central star(s) at position $p^{star}$. Considering single scattering only, $S(v)$ is computed as

$$S(v) = \phi(c,v,p^{star})L_e^{star} \cdot e^{-\int_{p^{star}}^v \tau(w)dw} \quad (2)$$
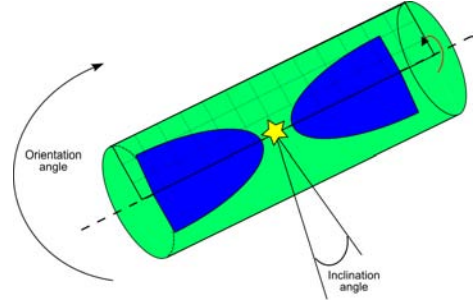
**Figure 3:** *The axis-symmetric model of a planetary nebula. The* orientation angle *determines the rotation of the nebulas axis of symmetry in the plane perpendicular to the viewing direction. The* inclination angle *measures the tilt of the axis in relation to the viewing direction. A 3D volume of a nebula can be generated by rotating a 2D map around its axis of symmetry.*

incorporating the extinction on the way from the star to the voxel as well as the Henyey-Greenstein scattering phase function $\phi$ from the star to the voxel into the direction of the camera $c$. We assume the same phase function for all voxels. $\phi$, $L_e^{star}$, and $p^{star}$ are assumed to be known. For a many nebulae they can be looked up in the astrophysical literature.

The extinction $\tau(v)$ and the albedo $\sigma(v)$ are directly proportional to the dust density $d_{dust}(v)$, while $L_e(v)$ is linearly related to the concentration of ionized gas $d_{gas}(v)$. The exact factors can be found in physics textbooks. The goal is to determine $d_{dust}(v)$ and $d_{gas}(v)$ up to scale.

Reconstructing a 3D volume based solely on a single 2D view is generally an ill-posed problem. Using the axial symmetry constraint we can simplify the problem of reconstructing a 3D volume to that of reconstructing a 2D map. This reduces the complexity of the reconstruction problem and speeds up the optimization process. At each step in the reconstruction, a 3D volume is obtained from the 2D maps by rotating the maps around the symmetry axis, see Figure 3. During the description of the algorithm, to better distinguish between reference images and the reconstructed 2D slices, we will refer to 2D recordings of real nebulae as *images*, and to the reconstructed 2D axis-symmetric distributions as *maps*.

### 3.1. Optimization

To drive our optimization we use the standard implementation of Powell's non-linear optimization method [PTVF92]. At every step, the sum of squared differences between the rendered and the reference image is evaluated. The algorithm minimizes this error functional by updating individual pixels in the maps and stops when it drops below a given threshold. We always initialize the maps to be zero. Besides the values in the 2D map, the algorithm also optimizes the inclination and orientation angles of the nebula (Figure 3). An initial

estimate for the orientation angle is computed based on the input images by calculating the principal eigenvectors of the image's covariance matrix. The initial inclination angle is set to 90°, i.e. symmetry axis is parallel to the image plane.

Since each iteration step in the optimization requires the computation of a volume rendered image we exploit graphics hardware for acceleration. The rendering algorithm used is described in more detail in Section 4. We evaluate Equation 1 in each iteration step for the entire image, or use simplified versions (Equation 4 or Equation 5 in the particular cases below), and finally compute the difference to the reference image on a graphics card. The rest of the optimization is still controlled by the CPU though.

For a more efficient and more stable optimization we perform the optimization hierarchically, start by optimizing a low resolution map, successively increasing the resolution until it slightly exceeds the resolution of the input images.

### 3.2. Planetary Nebula Reconstruction

In order to reconstruct both *gas* and *dust* distributions, our algorithm needs as input two different images for each nebula. As a general prerequisite, these images have to be affected differently by the optical characteristics of the gas and dust elements present in the nebula.

### 3.2.1. Reconstruction Based on Radio and Visible Datasets

In this approach we use a pair of radio and visible wavelength images. The first input image (denoted as $U$) is a radio continuum image from which we derive the gas distribution $d_{gas}$. The radio data is not affected by the dust distribution at all. The radio intensity $U$ is related to the expected visible emission $U'$ of the gas by the following equation [LK05]

$$U' = 6.85 \cdot 10^{-10} \cdot v \cdot U \qquad (3)$$

where $v$ is the frequency of the radio observation in $GHz$ and $U$ is measured in $Jy$. We compute $U'$ which would correspond to an image of the nebula at the wavelength of $H\alpha$ emission of the ionized gas as if no dust were present (Figure 5, left). The second input image , denoted $A$ (Figure 6, left), is a captured image at this particular narrow band of visible wavelength corresponding to the same emissive $H\alpha$ gas elements which in fact is affected by scattering and absorption due to the dust.

*Gas distribution estimation.*

In the first step, the *emission density map* corresponding to the ionized gas distribution $d_{gas}(v)$ is reconstructed using $U'$ as reference image. The rendering model simplifies to

$$L(x,y) = \int_c^\infty L_e(v)dv \qquad (4)$$

because this observation is almost unaffected by the dust, so no absorption or scattering needs to be considered. The
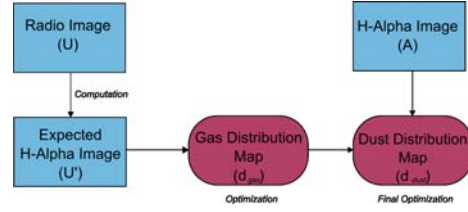


**Figure 4:** *Flowchart of the reconstruction process using radio and visible wavelength data. First, the radio input image is converted to simulate a visible wavelength image $U'$ of the emissive gas without any absorption or scattering. From $U'$ we derive $d_{gas}$. Using the visible wavelength image $A$ which capture the combined effects of the gas emission and the scattering and absorption of the dust, we obtain $d_{dust}$.*

gas distribution map is estimated using the iterative non-linear optimization algorithm (Section 3.1). Given a current estimate of the gas density map $d_{gas}$, the emission $L_e(v)$ is computed and an image is rendered according to Equation 4. The optimization drives the difference between this estimated image and the reference image $U'$ to a minimum. We initialize the optimization with a homogeneous distribution. Figure 5 shows the reference image $U'$, the recovered gas density map $d_{gas}$ and the rendering of the reconstructed volume. The reconstruction resembles the input up to the non-symmetries in the input.

*Dust distribution estimation.*

Using the gas density map $d_{gas}$ from the previous step and the image $A$ as reference, we optimize the *dust density map* until the reconstructed model resembles the reference image $A$. In this optimization step the nebula is rendered taking scattering and absorption into account as described by Equation 1. This time, the emission is derived from $d_{gas}$, while $d_{dust}$ accounts for scattering and absorption. In this process, the emission density map $d_{gas}$ recovered in step 1 is not optimized anymore. The results of this final optimization step are shown in Figure 6.

### 3.2.2. Reconstruction Based on Infrared and Visible Datasets

In this approach we use a pair of infrared and visible wavelength images. The first infrared input image, denoted $I$ (Figure 8, left), traces predominantly the dust particles present in the nebula, due to its intrinsic blackbody radiation. The second image, denoted $A$ (Figure 9, left), is again captured at visible wavelengths with a narrow-band $H\alpha$ filter. It shows the emission of the ionized gas and is affected by scattering and absorption due to the dust. In Figure 7, an overview of the reconstruction process using infrared and visible datasets is given. We first reconstruct the dust density map $d_{dust}$ using the infrared image $I$. In a second step, the gas density map $d_{gas}$ is optimized, until the rendering of the reconstruction which considers the effects of scattering and absorption due to dust resembles the visible wavelength input image $A$.
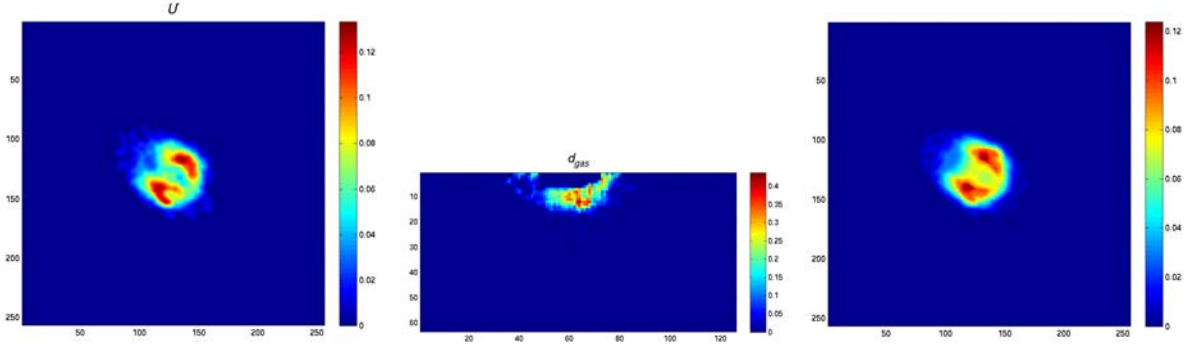
**Figure 5:** *Left: Input image for the M3-35 planetary nebula, corresponding to U′. Middle: Recovered gas density map $d_{gas}$. Right: Rendering of the reconstruction. Some deviations are visible because the input is not perfectly symmetric.*
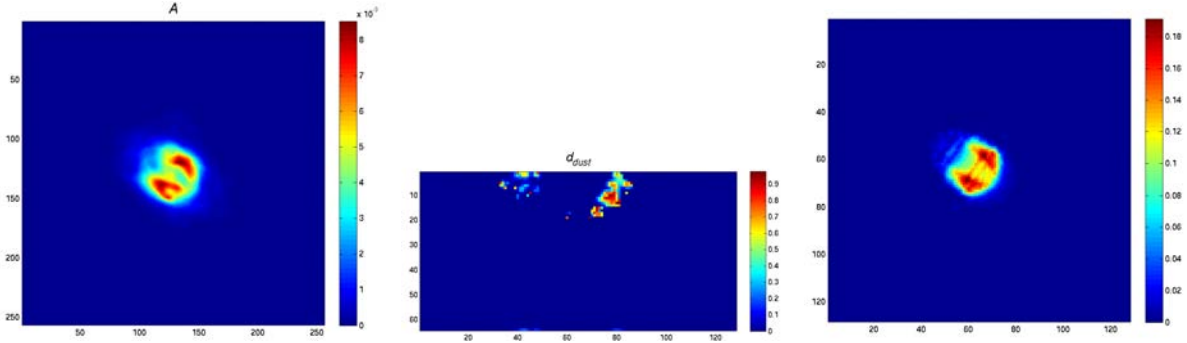


**Figure 6:** *Left: Hα image of the M3-35 planetary nebula, corresponding to A. The symmetry axis in this figure as well as in U′ from Figure 5 spans from the upper left to the lower right corner. Middle: Final recovered $d_{dust}$ dust map. Right: Rendering of the final reconstruction, considering absorption and scattering.*
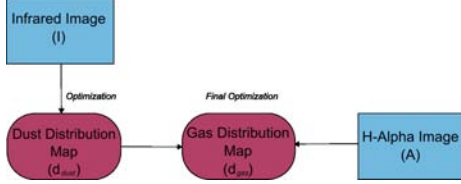


**Figure 7:** *Overview of the reconstruction process using infrared datasets. $d_{dust}$ is estimated from infrared image which corresponds to the black-body emission of the dust. The combined effect of dust absorption and scattering, and the gas emission is captured in A, from which $d_{gas}$ can be derived.*

### Dust distribution estimation.

In the first step, the *dust density map* corresponding to the dust particles present in the nebula $d_{dust}$ is reconstructed using $I$ as reference image. Because at certain infrared wavelengths electromagnetic emission is proportional only to the dust's intrinsic temperature, we can consider the dust particles being emissive, and the rendering model for infrared observations simplifies to

$$L_{dust}(x,y) = \int_c^\infty L_I^{dust}(v)dv \qquad (5)$$

where $L_{dust}(x,y)$ is the measured infrared radiance at position $(x,y)$ and $L_I^{dust}(v)$ is the infrared emission of the dust particles. The dust distribution map is estimated using the same iterative non-linear optimization algorithm which has been applied in Section 3.2.1 in order to estimate the emissive gas distribution. Figure 8 shows the reference image $I$, the recovered dust density map $d_{dust}$ and the rendering of the reconstructed volume.

### Gas distribution estimation

In this second step, using the dust distribution map $d_{dust}$ from the previous step, and image $A$ as a reference, we optimize the gas distribution map $d_{gas}$ until the rendering of the model resembles image $A$. In this second step, the dust is no longer treated being emissive and we render the nebula taking into account absorption and scattering as described by Equation 1. The result of the reconstruction process in shown in Figure 9.

## 4. Rendering and Visualization

To visualize the results of the reconstruction we adapted the OpenGL based renderer used for reflection nebulae visualization by Magnor et al. [MHLH05]. It is a volume rendering application based on a real time ray-caster implemented on graphics hardware. The implemented algorithm uses the
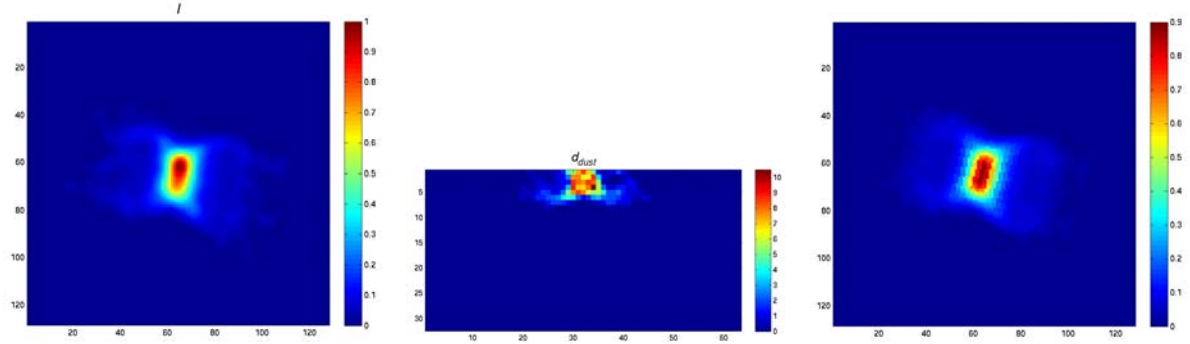
**Figure 8:** *Left: Input image for the Hen 2-320 planetary nebula, corresponding to I. The axis of symmetry spans almost horizontally across the image with a slight tilt. Middle: Recovered dust density map $d_{dust}$. Right: Rendering of the reconstruction.*
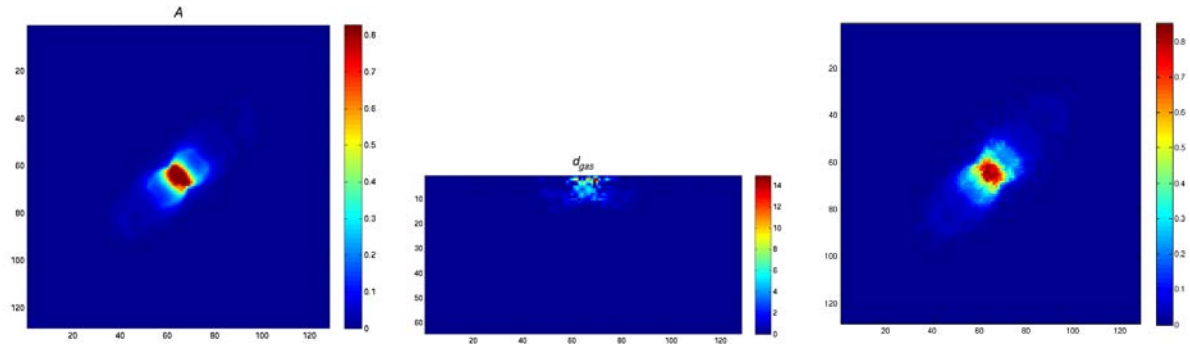


**Figure 9:** *Left: Hα input image corresponding to A. The axis of symmetry spans over the diagonal from the lower left to the upper right corner. Middle: Recovered gas density map $d_{gas}$. Right: Rendering of the final reconstruction, considering absorption and scattering.*



**Figure 10:** *2D Precomputation of the light reaching a voxel (striped texel) from the central star within the map instead of computing it for the full volume. All dust density values on the line from the central star to the texel are accumulated.*

idea described by Krüger et al. [KW03] to color code the direction of the viewing rays using a bounding box. In the next step, we exploit modern graphics hardware's capabilities to step along the lines of sight querying 3D textures using a fragment shader to accumulate the emission and inscattering along each ray while considering absorption. To further increase the frame rate of the interactive visualization tool we extended the existing renderer by implementing *empty space skipping* [SA95] to improve the volume's bounding geometry.

As another optimization for the rendering, we partially precompute the single scattering term (Equation 2) within

the map instead of the full volume. The integral $\tau(x,y) = e^{-\int_{p^{star}}^{y} \tau(w)dw}$ can be fully determined within the 2D map (see Figure 10), which is then rotated around the symmetry axis to compute the inscattering to each voxel. To the final output, we apply gamma correction and high dynamic range rendering. We achieve about 14 fps, at $128 \times 128$ resolution.

## 5. Results

We have applied the proposed pipelines to two different data sets, a pair of radio and visible wavelength images for the nebula M3-35 and a pair of infrared and visible wavelength images for the nebula Hen 2-320. Computation times for both nebulae range in the scale of 24 hours per dataset / wavelength.

For the approach based on radio and visible wavelengths presented in Section 3.2.1, we used data from the paper by Lee et al. [LK05], consisting of observations of PNe in the visible wavelengths from the Hubble Space Telescope (HST) and radio data from the Very Large Array radio observatory. These are compact planetary nebulae with a symmetrical form.

For the approach based on datasets at infrared and visible

wavelengths described in Section 3.2.2, we combined an infrared dataset kindly provided by Kevin Volk, Gemini Observatory, and visible observations taken with the HST, which are publicly available from the HST Online Arcive [NAS07].

Because we make use of datasets from different telescopes for the same astronomical object we had to align and to scale the radio / infrared data to match the visible wavelength images. This is necessary because of the positioning uncertainties and the different resolutions of the given telescopes.

In addition, we were not able to obtain absolutely photometrically calibrated images. We therefore included a relative intensity scale between the gas emission and the dust absorption, and the overall intensity of the central star into our optimization scheme, adding two global scalar parameters. Using additional calibration data this step could be avoided in order to obtain absolute dust and gas densities which we so far can only estimate up to some unknown factor.

### 5.1. Planetary Nebula M3-35

For the volumetric reconstruction of the planetary nebula M3-35 based on radio and visible wavelength images results are shown in Figures 5 and 6. Our algorithm recovered for this nebula an inclination angle of $73°$, which is fairly close to the value of $80°$ given in [LK05]. The reconstructed gas density map $d_{gas}$ (Figure 5, middle) highlights an area of low gas density in the center which corresponds to the input radio map. Because of the slightly asymmetric shape of the real nebula there are however some small deviations in the red top right region. The recovered dust map (Figure 6) correctly attenuates the intensity of the bottom right part of the nebula.

### 5.2. Planetary Nebula Hen 2-320

The reconstruction results for planetary nebula Hen 2-320 based on infrared and visible wavelength images are shown in Figures 8 and 9. Our algorithm recovered an inclination angle of $90°$, indicating that the symmetry axis is parallel to the image plane. The reconstructed dust density map $d_{dust}$ (Figure 8, middle) reproduces the nebulas butterfly-like lobes visible in the infrared image $I$ very well, up to the asymmetries of the red center.

Results from the gas reconstruction are presented in Figure 9. The map $d_{gas}$ (Figure 9, middle) also succeeds to recover the two butterfly like lobes noticeable in the $H\alpha$ input image $A$. Currently, we observe slight block artifacts in the final rendering, which might be due to the accumulated effect of the two subsequent optimization steps and their specific errors, which influence each other in a non-linear way. Still, the main structures of the nebula are well represented, indicating a plausible reconstruction. The artifacts can be reduced if smoothness is enforced during the optimization of the gas map.
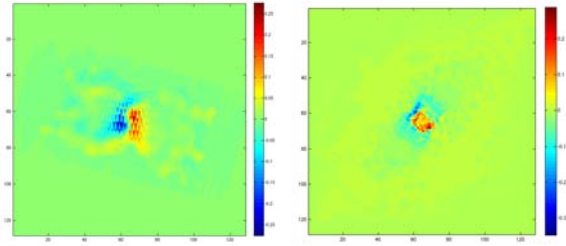


**Figure 11:** *Difference between the input images and the reconstructions for nebula Hen 2-320. Left: for the density reconstruction in Figure 8. Right: for the gas reconstruction in Figure 9.*
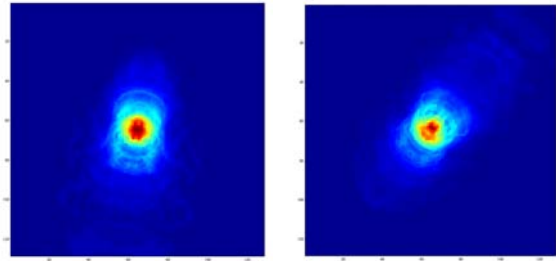


**Figure 12:** *Reconstructed He2-320 rendered at an inclination angle of $50°$ and $75°$. By viewing the nebula at different inclination angles, we can derive a better insight in its 3D distribution.*

Figure 11, left, shows the difference images after the reconstruction of the dust distribution and respectively right, after the final optimization of the gas distribution. The RMS errors for the $128 \times 128$ input images are relatively low: 0.0172 and 0.0153, respectively.

From the recovered distributions we can now render the nebula from different view points (inclination angles) as presented in Figure 12. The synthesized images provide novel ways for exploring the 3D structure of the nebula.

### 6. Discussion and Future Work

The presented results demonstrate the effectiveness of our volumetric reconstruction algorithm for planetary nebulae. Given two input images at different wavelengths, we can recover both the 3D distribution of emitting gas as well as the density of dust particles in axis-symmetric nebulae. Our physically-based reconstruction and visualization algorithms simulate emission, absorption and scattering.

The quality of the reconstruction results is limited by the input images for any recovered gas or dust data. It is important that the input images are well aligned and have similar resolution in order to obtain accurate reconstruction results. Furthermore, any deviation from axis-symmetry in the real nebula affects the reconstructed volumes.

Because we assume axial-symmetry the reconstruction re-

sults depend on the inclination angle of the symmetry axis and the projection direction. The best quality is obtained if the symmetry axis is parallel to the image plane.

While our current approach incorporates only two images at different wavelengths and assumes that the image of one wavelength is not at all effected by the dust, further extension of the algorithm could incorporate more images at different wavelengths to increase the stability of the optimization. In addition, it is not necessary to assume that one image is completely unaffected by scattering and absorption. As long as the scattering and absorption coefficients are sufficiently different the ionized gas and the dust distributions could be recovered if optimized simultaneously.

Besides the application in astronomy, it is promising to investigate the performance of the proposed volumetric reconstruction algorithm in the context of medical imaging, where scattering and absorption are the main effects when illuminating through biological tissue.

**Acknowledgements**

**References**

[BF02] BALICK B., FRANK A.: Shapes and Shaping of Planetary Nebulae. *Annual Review of Astronomy and Astrophysics 40* (2002), 439–486. 2

[GBH70] GORDON R., BENDER R., HERMAN G.: Algebraic Reconstruction Techniques (ART) for Three-dimensional Electron Microscopy and X-ray Phtography. *Journal of Theoretical Biology 29* (1970), 471–481. 1

[HG41] HENYEY L. G., GREENSTEIN J. L.: Diffuse Radiation in the Galaxy. *Astrophysical Journal 93* (1941), 70–83. 3

[KW03] KRÜGER J., WESTERMANN R.: Acceleration techniques for GPU-based volume rendering. In *14th IEEE Visualization 2003 Conference (VIS 2003), 19-24 October 2003, Seattle, WA, USA* (2003), Turk G., van Wijk J. J., II R. M., (Eds.), IEEE Computer Society, pp. 287–292. 6

[KWAH06] KAEHLER R., WISE J., ABEL T., HEGE H.-C.: GPU-assisted raycasting for cosmological adaptive mesh refinement simulations. In *Eurographics/IEEE VGTC Workshop on Volume Graphics* (Boston, Massachusetts, USA, 2006), Machiraju R., Möller T., (Eds.), Eurographics Association, pp. 103–110. 1

[Kwo00] KWOK S.: *The Origin and Evolution of Planetary Nebulae*. Cambridge ; New York : Cambridge University Press, 2000. (Cambridge astrophysics series ; 33), June 2000. 2

[LK05] LEE T.-H., KWOK S.: Dust Extinction in Compact Planetary Nebulae. *The Astrophysical Journal 632* (Oct. 2005), 340–354. 2, 4, 6, 7

[MHLH05] MAGNOR M., HILDEBRAND K., LINŢU A., HANSON A. J.: Reflection Nebula Visualization. In *Proceedings of the IEEE Conference on Visualization (VIS'05)* (Minneapolis, USA, Oct. 2005), Silva C., Gröller E., Rushmeier H., (Eds.), IEEE, pp. 255–262. 2, 5

[MKHD04] MAGNOR M., KINDLMANN G., HANSEN C., DURIC N.: Constrained inverse volume rendering for planetary nebulae. In *Proc. IEEE Visualization 2004, Austin, USA* (Oct. 2004), pp. 83–90. 1, 2

[NAS07] NASA: Hubble Space Telescope Online Archive. available from archive.stsci.edu/hst/search.php, 2007. 7

[NGN*01] NADEAU D. R., GENETTI J. D., NAPEAR S., PAILTHORPE B., EMMART C., WESSELAK E., DAVIDSON D.: Visualizing stars and emission nebulas. *Comput. Graph. Forum 20*, 1 (2001), 27–33. 1

[Ost74] OSTERBROCK D. E.: *Astrophysics of gaseous nebulae*. San Francisco, W. H. Freeman and Co., 1974. 263 p., 1974. 2

[PTVF92] PRESS W. H., TEUKOLSKY S. A., VETTERLING W. T., FLANNERY B. P.: *Numerical Recipes in C: The Art of Scientific Computing*, 2. ed. Cambridge University Press, Cambridge, MA, 1992. 3

[SA95] SOBIERAJSKI L. M., AVILA R. S.: A Hardware Acceleration Method for Volumetric Ray Tracing. In *IEEE Visualization* (1995), p. 27. 6

[SAP*02] SHARPE J., AHLGREN U., PERRY P., HILL B., ROSS A., HECKSHER-SORENSEN J., BALDOCK R., DAVIDSON D.: Optical Projection Tomography as a Tool for 3D Microscopy and Gene Expression Studies. *Science 296*, 19 (2002). 1

[TBH06] TRIFONOV B., BRADLEY D., HEIDRICH W.: Tomographic reconstruction of transparent objects. In *Rendering Techniques 2006: 17th Eurographics Workshop on Rendering* (2006), pp. 51–60. 1